Chemical Science

ROYAL SOCIETY OF CHEMISTRY

EDGE ARTICLE

View Article Online
View Journal

Cite this: DOI: 10.1039/d6sc02482c

All publication charges for this article have been paid for by the Royal Society of Chemistry

Interface charge engineering of ternary RuCoMo oxide nanofibers toward high-current-density water electrolysis

Linfeng Zhang,†[a] Mingze Xia,†[a] Weimo Li,*[b] Siyu Ren,[a] Li Deng,[a] Siqi Zhang,[a] Lin Huang,[a] Wei Song [c] and Xiaofeng Lu *[a]

Received 26th March 2026
Accepted 8th June 2026

DOI: 10.1039/d6sc02482c

rsc.li/chemical-science

The efficacy of RuO_2 as a bifunctional electrocatalyst for alkaline water electrolysis is usually constrained by its sluggish hydrogen evolution kinetics and poor stability. Herein, we report the fabrication of ternary $RuCoMoO_x$ nanofibers (NFs) incorporating oxide heterojunctions, which address these issues through interfacial charge engineering. The electron redistribution induced by the constructed interface optimizes the local electronic environment, endowing the catalyst with superior activity and stability for both the hydrogen and oxygen evolution reactions (HER/OER). The $RuCoMoO_x$ NFs require ultralow overpotentials of 274.8 mV for the HER and 367.9 mV for the OER to deliver a high current density of 1 A cm^{-2}, surpassing commercial Pt/C and RuO_2 benchmarks. Moreover, the catalyst possesses superior operational stability for both the HER and the OER at 1 A cm^{-2} compared to Pt/C and RuO_2, respectively. In a practical electrolyzer, the assembled symmetric $RuCoMoO_x$ NFs||$RuCoMoO_x$ NFs system delivers a much lower working voltage than Pt/C||RuO_2 and maintains stable operation at 1 A cm^{-2} for 60 h. This work validates interfacial charge engineering as a key strategy for creating high-performance noble-metal-lean electrocatalysts for industrial water electrolysis.

Introduction

The global energy crisis and the exacerbation of climate change, driven by greenhouse gas emissions from excessive fossil fuel consumption, have intensified the demand for sustainable low-carbon energy alternatives.[1–3] In this context, electrochemical water splitting powered by renewable electricity has consequently emerged as a pivotal carbon-neutral technology for hydrogen (H_2) production. The efficiency of this process is governed by the hydrogen evolution reaction (HER) and the oxygen evolution reaction (OER), placing critical demands on the development of highly efficient and robust electrocatalysts.[4,5] Although noble metal-based catalysts (*e.g.*, Pt/C and IrO_2) currently dominate industrial electrocatalytic water splitting, their prohibitive costs and limited availability severely restrict widespread implementation. Therefore, the development of cost-effective and sustainable alternatives has become an urgent priority.[6,7]

To address the cost and scarcity constraints of noble metal-based catalysts, recent research has focused on innovative designs that minimize noble metal loading while maintaining or even enhancing catalytic performance.[8,9] Strategies such as interface engineering and crystal-phase modulation enable atomic-level electronic structure tailoring, generating highly active sites with enhanced catalytic functionality.[10–12] In particular, heterojunction construction promotes interfacial charge redistribution, which optimizes the electronic environment of the catalyst and improves its intrinsic activity. The synergistic effects between components often yield performance enhancements that surpass those of individual-component catalysts.[13–15] Among various candidate materials, ruthenium-based oxides (*e.g.*, RuO_2) have attracted significant interest due to their exceptional alkaline OER activity, yet face deployment barriers from high cost and insufficient stability at industrial current densities.[16–18] In contrast, $CoMoO_4$ presents a cost-effective alternative for the OER, featuring multivalent characteristics, a tunable electronic structure, and favorable intermediate adsorption energetics.[19–21] Although β-$CoMoO_4$ has been fabricated *via* a hydrothermal method and exhibits favorable OER activity with an overpotential of 366 mV at 10 mA cm^{-2} in alkaline electrolyte, its OER activity remains intrinsically lower than that of noble-metal catalysts. Furthermore, its HER performance is limited by suboptimal H* adsorption energetics. Consequently, the implementation of $CoMoO_4$ as

[a]Alan G. MacDiarmid Institute, College of Chemistry Jilin University, Changchun 130012, P. R. China. E-mail: xflu@jlu.edu.cn

[b]Department of Materials Science and Engineering, Zhejiang Normal University, Yingbin Road 688, Jinhua 321004, P. R. China. E-mail: liweimo@zjnu.edu.cn

[c]State Key Laboratory of Supramolecular Structure and Materials, College of Chemistry, Jilin University, Changchun 130012, P. R. China

† These authors contribute equally to this work.

a bifunctional catalyst for overall water splitting remains constrained.[22]

Herein, we propose an interfacial engineering strategy to construct ternary $RuCoMoO_x$ nanofibers (NFs) featuring RuO_2/$CoMoO_4$ heterojunctions as a bifunctional electrocatalyst for water electrolysis. This design leverages interfacial electronic interactions and synergistic effects to achieve highly efficient and stable electrocatalytic performance. This unique configuration not only exposes abundant catalytically active interfaces that facilitate rapid charge transfer and redistribution, thereby optimizing the electronic states of the active sites, but also benefits from the continuous fibrous morphology to promote efficient axial electron transport along the NFs. The synergistic interplay endows $RuCoMoO_x$ NFs with remarkable bifunctional activity in alkaline media, achieving ultralow overpotentials of only 274.8 mV for the HER and 367.9 mV for the OER at 1 A cm^{-2}, along with outstanding industrial stability. When assembled into a $RuCoMoO_x$ NFs||$RuCoMoO_x$ NFs electrolyzer for overall water splitting (OWS), the system delivers a much lower working voltage and more robust operation than its commercial Pt/C||RuO_2 counterpart. Density functional theory (DFT) calculations reveal that substantial electron redistribution across the RuO_2/$CoMoO_4$ interface effectively activates Co sites for the OER while optimizing Ru sites for the HER, thereby reducing the kinetic barriers and enhancing overall catalytic activity. This work demonstrates that coupling interfacial charge engineering with a nanofibrous architecture can overcome the limitations of single-metal oxides, providing a viable path to noble metal-lean electrocatalysts that meet industrial-current-density requirements for both activity and durability in alkaline water electrolysis.

Results and discussion

Electrospinning offers a versatile strategy that enables the fabrication of nanofibers.[23–25] As depicted in Fig. 1a, precursor NFs containing $RuCl_3$, $Co(NO_3)_2$ and molybdenum acetylacetonate dispersed in a polyvinylpyrrolidone (PVP) matrix are fabricated *via* electrospinning, yielding a uniform fibrous structure with an average diameter of approximately 198.8 nm (Fig. S1, SI). After calcination at 550 °C, field-emission scanning electron microscopy (FESEM) and transmission electron microscopy (TEM) images show sintering-induced shrinkage of the resulting $RuCoMoO_x$ NFs, with the average diameter decreasing to 111.9 nm, attributable to the decomposition of PVP (Fig. 1b–d). Meanwhile, deliberate variation of the Ru molar content in $RuCoMoO_x$ NFs shows that the uniform nanofibrous morphology is maintained across all compositions (Fig. S2–S5, SI). In addition, a systematic investigation of the calcination temperature reveals that increasing the temperature from 450 °C to 650 °C leads to significantly enhanced surface roughness of the nanofibers (Fig. S6 and S7, SI). The X-ray diffraction (XRD) pattern of $RuCoMoO_x$ NFs confirms the presence of both tetragonal RuO_2 (JCPDS no. 43-1027) and monoclinic $CoMoO_4$ (JCPDS no. 21-0868), providing evidence for the successful

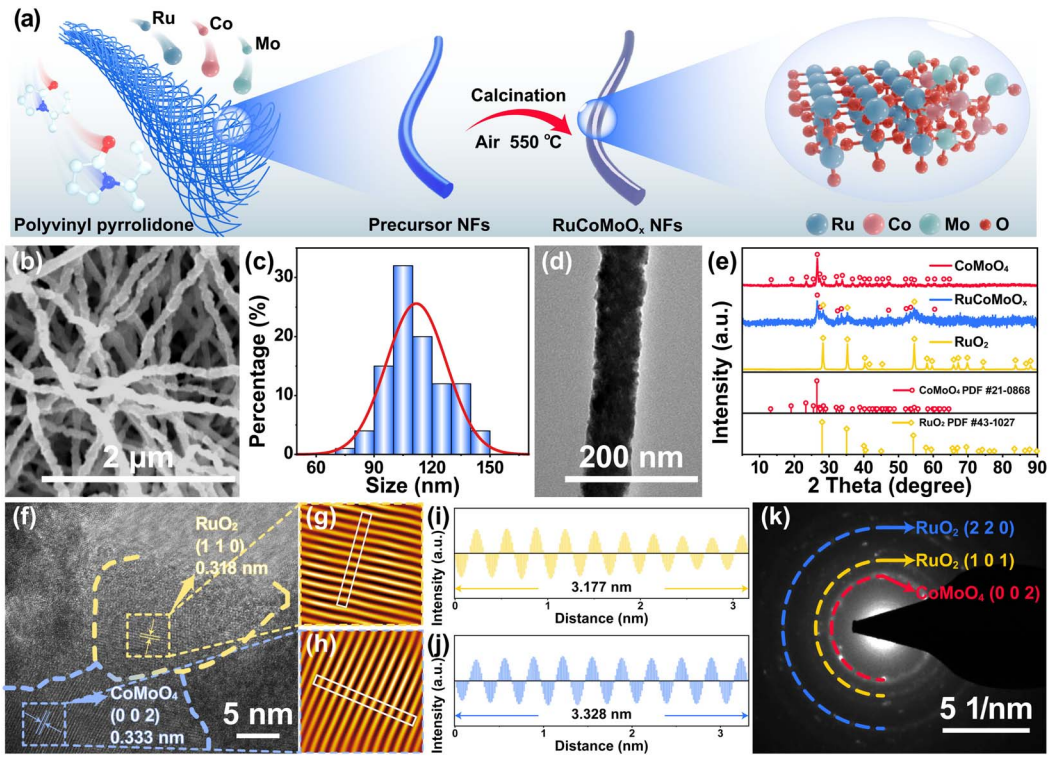

Fig. 1 (a) Schematic illustration of the synthetic procedure for $RuCoMoO_x$ NFs. (b) SEM image, (c) fiber diameter distribution, and (d) TEM image of $RuCoMoO_x$ NFs. (e) XRD patterns of $CoMoO_4$ NFs, $RuCoMoO_x$ NFs, and RuO_2 NFs. (f) HRTEM image of $RuCoMoO_x$ NFs with fast Fourier transform (FFT) patterns and lattice fringes of (g and i) RuO_2 (110) and (h and j) $CoMoO_4$ (002) crystal planes. (k) SAED pattern of $RuCoMoO_x$ NFs.

formation of the $RuO_2/CoMoO_4$ composite (Fig. 1e).[26–28] With increasing Ru precursor loading, the intensity of the RuO_2 diffraction peaks increases proportionally, indicating a higher phase fraction of RuO_2 (Fig. S8a, SI). At a fixed Ru : Co : Mo molar ratio of 1 : 1 : 1, raising the calcination temperature from 450 °C to 650 °C results in progressively sharper and more intense diffraction peaks, reflecting improved crystallinity and larger average crystallite sizes (Fig. S8b, SI). In addition, the N_2 adsorption–desorption isotherm demonstrates that the $RuCoMoO_x$ NFs exhibit a Brunauer–Emmett–Teller (BET) surface area of 24.88 $m^2 g^{-1}$ (Fig. S9, SI), which is similar to that of previous reported electrospun nanofibers.[29,30]

High-resolution TEM (HRTEM) imaging of the $RuCoMoO_x$ NFs reveals distinct lattice fringes with measured spacings of 0.318 nm and 0.333 nm (Fig. 3f), which are assigned to the (110) plane of RuO_2 and the (002) plane of $CoMoO_4$, respectively. The formation of a well-defined heterointerface between these two phases is evidenced, supported further by the corresponding fast Fourier transform (FFT) analyses (Fig. 1g–j).[31–33] Additionally, the selected area electron diffraction (SAED) pattern displays characteristic diffraction rings indexed to the (101) and (200) planes of RuO_2 alongside the (002) facet of $CoMoO_4$ (Fig. 1k). Energy-dispersive X-ray (EDX) analysis confirms the elemental composition of the as-prepared $RuCoMoO_x$ NFs, with C, Cu, and Si signals originating from the TEM grid and instrumentation (Fig. S10, SI). The EDX result further shows that the molar ratio of Ru : Co : Mo is 9.21 : 9.64 : 8.21, which is nearly identical to their feeding ratio. Collectively, these complementary structural characterization results collectively validate the successful integration of $RuO_2(110)/CoMoO_4(002)$ heterojunctions into the $RuCoMoO_x$ NFs, providing a robust structural basis for exploring interfacial electronic redistribution and its influence on electrocatalytic performance.

To gain deeper insight into the surface chemical states and interfacial electronic interactions within the catalysts, X-ray photoelectron spectroscopy (XPS) analysis is conducted. The survey spectra (Fig. 2a) confirm the successful incorporation of all constituent elements into the catalysts. In the O 1s region (Fig. 2b), $RuCoMoO_x$ NFs exhibit two distinct peaks centered at 530.6 eV and 529.6 eV, which correspond to the lattice oxygen in $CoMoO_4$ and RuO_2, respectively.[19,34] Notably, the binding energies of these lattice oxygen peaks are negatively shifted by 0.2 eV compared to pure $CoMoO_4$ and RuO_2. These negative shifts suggest significant interfacial charge redistribution, providing

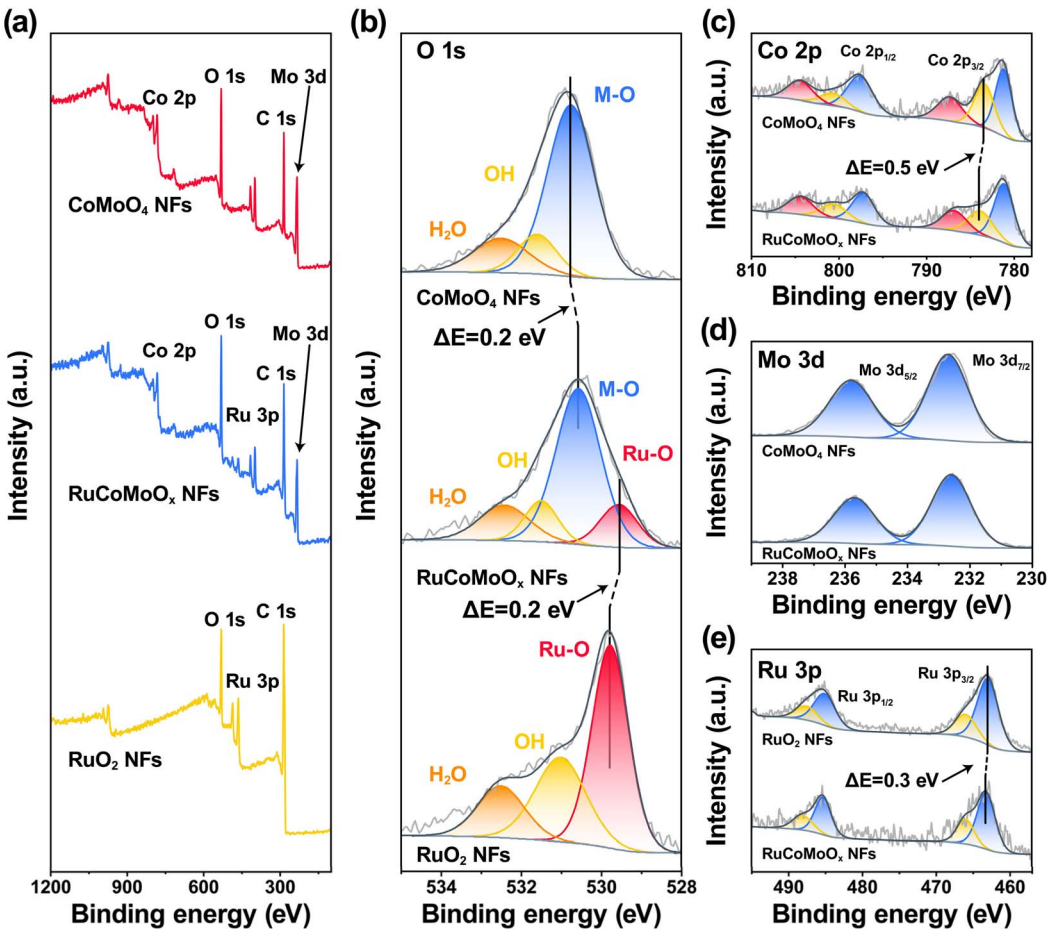

Fig. 2 XPS analysis of $CoMoO_4$ NFs, $RuCoMoO_x$ NFs, and RuO_2 NFs: (a) survey spectra and (b) high-resolution O 1s spectra. High-resolution spectra of (c) Co 2p for $CoMoO_4$ NFs and $RuCoMoO_x$ NFs, (d) Mo 3d for $CoMoO_4$ NFs and $RuCoMoO_x$ NFs, and (e) Ru 3p for RuO_2 NFs and $RuCoMoO_x$ NFs.

further evidence of strong electronic interactions between $CoMoO_4$ and RuO_2 within the heterostructure. The high-resolution Co 2p spectrum of pristine $CoMoO_4$ NFs displays the coexistence of Co^{2+} and Co^{3+} species, with the corresponding peaks located at 781.2 eV and 783.4 eV, respectively. In the $RuCoMoO_x$ NF heterostructure, the Co^{2+} $2p_{3/2}$ peak shifts positively by 0.5 eV to 783.9 eV relative to that of $CoMoO_4$ NFs, reflecting an altered electronic environment of Co^{2+} resulting from interfacial charge redistribution at the $CoMoO_4/RuO_2$ heterojunction (Fig. 2c).[35,36] For the Mo 3d region, both $CoMoO_4$ NFs and $RuCoMoO_x$ NFs exhibit only Mo^{6+} signals, with the Mo $3d_{5/2}$ and Mo $3d_{3/2}$ peaks at 232.5 eV and 235.6 eV, respectively. No significant binding energy shift is observed between the two samples (Fig. 2d).[37–40] The Ru 3p spectrum of pristine RuO_2 NFs features characteristic Ru^{4+} peaks at 462.9 eV (Ru $3p_{3/2}$) and 485.1 eV (Ru $3p_{1/2}$).[41,42] Upon heterostructure formation, the Ru $3p_{3/2}$ peak shifts positively by 0.3 eV, indicating a modified electronic environment of Ru arising from interfacial charge redistribution at the $RuO_2/CoMoO_4$ heterojunction (Fig. 2e).[43,44] Collectively, these XPS findings provide unambiguous evidence that the formation of a $RuO_2/CoMoO_4$ heterojunction induces charge redistribution, which effectively modulates the local electronic environment of the active sites, being responsible for the enhanced electrocatalytic activity.

We systematically evaluated the electrocatalytic HER performance of $RuCoMoO_x$ NFs alongside several control samples in 1.0 M KOH. Linear sweep voltammetry (LSV) profiles clearly demonstrate that $RuCoMoO_x$ NFs exhibit optimal HER properties, achieving a current density of 1 A cm^{-2} with an overpotential of only 274.8 mV, significantly lower than those of $CoMoO_4$ NFs (425.2 mV), $0.5RuCoMoO_x$ NFs (368.5 mV), $1.5RuCoMoO_x$ NFs (317.0 mV), RuO_2 NFs (324.9 mV), and commercial Pt/C (347.7 mV) (Fig. 3a). Optimization of the calcination temperature further confirms that $RuCoMoO_x$ NFs treated at 550 °C afford the best HER activity (Fig. S11, SI). When benchmarked against recently reported HER electrocatalysts, the $RuCoMoO_x$ NFs catalyst ranks among the top performers in terms of overpotential at 1 A cm^{-2}, highlighting its exceptional activity (Fig. 3b and Table S1, SI). Tafel analysis indicates superior HER kinetics for $RuCoMoO_x$ NFs, with a Tafel slope of 41.3 mV dec^{-1}, approaching that of commercial Pt/C (30.0 mV dec^{-1}) (Fig. 3c). Electrochemical impedance spectroscopy (EIS) further supports these findings, with the Nyquist plot of $RuCoMoO_x$ NFs exhibiting the smallest charge transfer resistance (R_{ct}) among the samples, suggesting the most rapid electron transfer kinetics (Fig. 3d). The EIS data are modeled using the equivalent circuits shown in Fig. S12, SI. The Bode plot (Fig. S13, SI) reveals distinct phase angle features, with the low-frequency region corresponding to the Volmer step and the

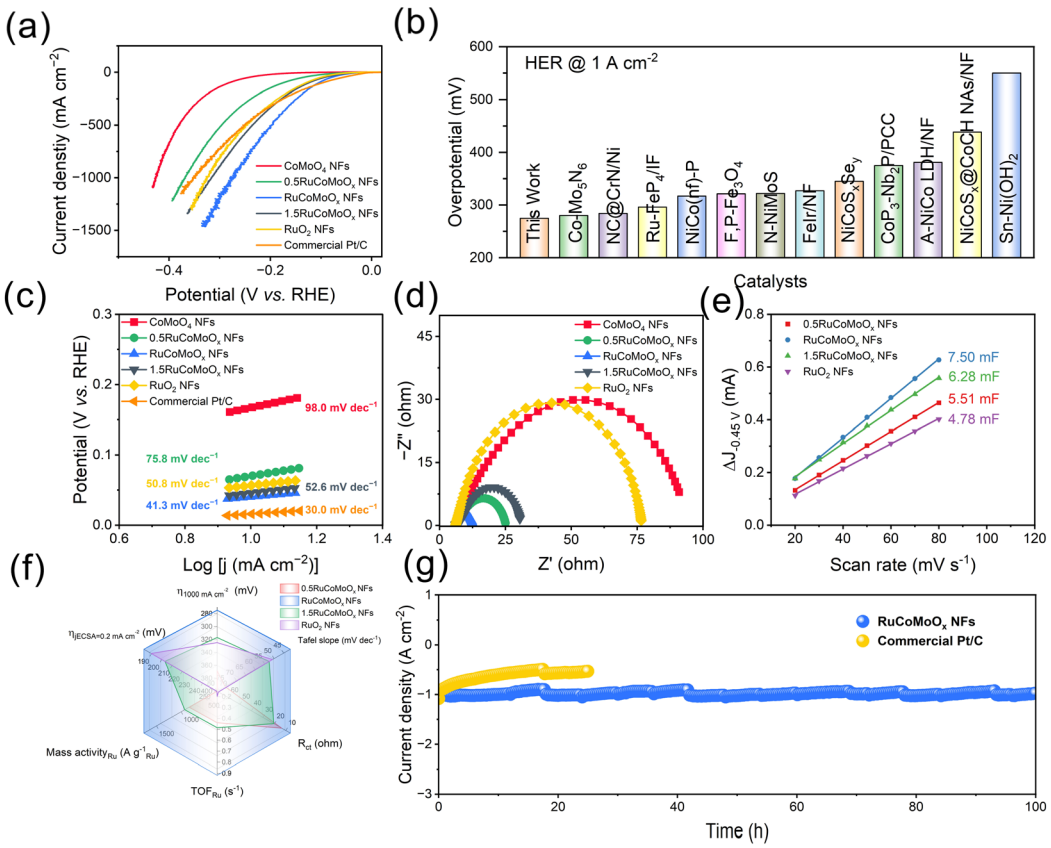

Fig. 3 HER performance in 1.0 M KOH. (a) LSV curves. (b) Performance comparison against state-of-the-art catalysts at 1 A cm^{-2}. (c) Tafel plots. (d) Nyquist plots. (e) C_{dl} values and (f) radar chart of $RuCoMoO_x$ NFs and control catalysts. (g) I–t curves of $RuCoMoO_x$ NFs and commercial Pt/C conducted at 1 A cm^{-2}.

mid-frequency region to the Heyrovsky step.[45,46] In addition, as the applied voltage decreases, the phase angle peaks in both the low- and mid-frequency regions progressively shift toward higher frequencies. This behavior is primarily ascribed to a reduction in charge transfer impedance at the catalyst surface/electrolyte interface and the acceleration of the interfacial reaction kinetics.[47,48]

The electrochemically active surface area (ECSA) is estimated from double-layer capacitance (C_{dl}) measurements derived from cyclic voltammograms (CVs) recorded at various scan rates (Fig. 3e and S14, S15, SI). $RuCoMoO_x$ NFs exhibit the largest C_{dl} value of 7.50 mF, corresponding to the highest ECSA value (Table S2). Concurrently, the specific activity of the catalyst is assessed by analyzing ECSA-normalized LSV curves. Among all samples, $RuCoMoO_x$ NFs show a favorable overpotential of 182.4 mV at a normalized current density of 0.2 mA $cm^{-2}{}_{ECSA}$, indicating that the high intrinsic activity originates from the formation of the heterointerface (Fig. S16 and S17, SI). Furthermore, $RuCoMoO_x$ NFs exhibit superior mass $activity_{Ru}$ and the highest turnover frequency (TOF) per-Ru site (TOF_{Ru}) at an overpotential of 200 mV (Fig. S18 and S19, SI), providing further evidence of accelerated HER kinetics and enhanced intrinsic catalytic activity. A radar chart summarizing six key HER performance metrics highlights the overall superiority of $RuCoMoO_x$ NFs (Fig. 3f). Long-term stability is assessed by chronoamperometry at 1 A cm^{-2} (Fig. 3g). Notably, the current density of $RuCoMoO_x$ NFs remains close to its initial value after 100 h of testing, whereas commercial Pt/C exhibits a significant performance degradation after only 25 h. Post-test characterization confirms the structural and chemical stability of $RuCoMoO_x$ NFs. Specifically, FESEM, TEM and HRTEM images show that the nanofibrous morphology and chemical structure are well preserved (Fig. S20 and S21, SI). XRD reveals only a slight decrease in crystallinity, and XPS spectra indicate negligible changes in the chemical states of each element (Fig. S22, SI). Collectively, these results affirm the outstanding activity and stability of $RuCoMoO_x$ NFs as an efficient HER electrocatalyst.

Inspired by the enhanced HER performance achieved through interface engineering in $RuCoMoO_x$ NFs, the OER performance of the catalysts is also evaluated in alkaline media. Under optimized synthesis conditions, $RuCoMoO_x$ NFs calcined at 550 °C exhibit optimal OER activity, with an overpotential of 270.5 mV at 100 mA cm^{-2}, considerably lower than those of $CoMoO_4$ NFs (393.4 mV), RuO_2 NFs (717.6 mV) and commercial RuO_2 (733.2 mV) (Fig. 4a and S23, SI). Remarkably, $RuCoMoO_x$ NFs require only 367.9 mV to reach an industrial-level current density of 1 A cm^{-2}, surpassing most reported state-of-the-art alkaline OER catalysts (Fig. 4b and Table S3, SI). Furthermore, $RuCoMoO_x$ NFs show the lowest Tafel slope of 58.2 mV dec^{-1}

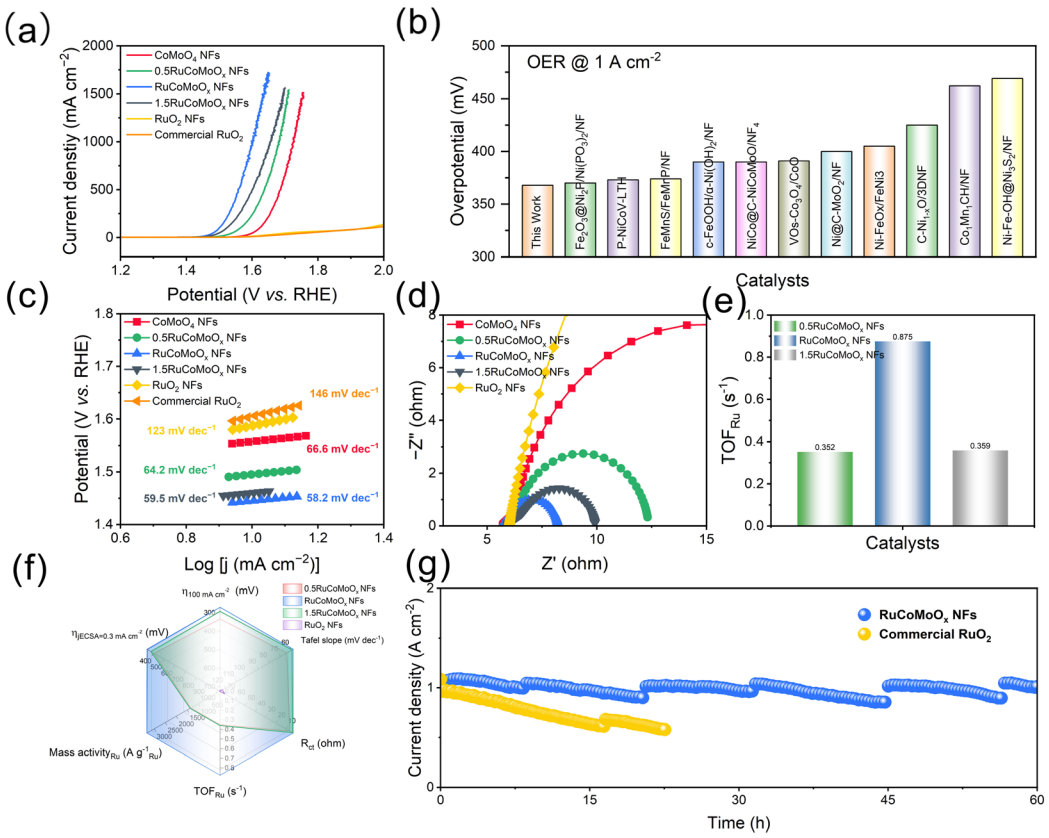

Fig. 4 OER performance in 1.0 M KOH. (a) LSV curves. (b) Performance comparison against state-of-the-art catalysts at 1 A cm^{-2}. (c) Tafel plots. (d) Nyquist plots. (e) TOF values at $\eta = 370$ mV based on the Ru feeding content. (f) Radar chart of $RuCoMoO_x$ NFs and other control catalysts. (g) I–t curves of $RuCoMoO_x$ NFs and commercial RuO_2 conducted at 1 A cm^{-2}.

among the tested catalysts, indicating favorable OER kinetics (Fig. 4c). EIS further reveals that $RuCoMoO_x$ NFs possess the lowest R_{ct} of 2.32 Ω, suggesting highly efficient electron transfer that underpins their outstanding OER performance (Fig. 4d). The Bode plot (Fig. S24. SI) shows that the smaller phase peak angle of $RuCoMoO_x$ NFs in the low frequency region of the *operando* Bode phase plots indicates that, during the OER process, $RuCoMoO_x$ NFs with $RuO_2/CoMoO_4$ heterojunctions exhibit faster charge transfer compared to RuO_2 NFs and $CoMoO_4$ NFs, leading to rapid OER kinetics.[32,48] The specific activity is assessed using ECSA-normalized LSV curves to investigate the intrinsic activity of catalysts. $RuCoMoO_x$ NFs demonstrate the highest intrinsic activity, with a low overpotential of 339.4 mV at 0.3 mA cm^{-2}_{ECSA} (Fig. S25 and S26, SI). Moreover, $RuCoMoO_x$ NFs deliver the highest TOF_{Ru} of 0.875 s^{-1} at 370 mV and a mass activity of 3346.49 A g^{-1}_{Ru} (Fig. 4e, S27 and Fig. S28, SI), reflecting accelerated OER kinetics and superior catalytic efficiency. Integration of six key metrics in the radar chart conclusively demonstrates the comprehensive superiority of $RuCoMoO_x$ NFs for the OER (Fig. 4f). A long-term chronopotentiometry test at 1 A cm^{-2} reveals excellent operational stability of the $RuCoMoO_x$ NFs, which retain a current density comparable to their initial value after 60 h, whereas that of commercial RuO_2 declines rapidly after 22.5 h under identical conditions (Fig. 4h). Post-stability characterizations further corroborate the structural and chemical robustness of $RuCoMoO_x$ NFs. SEM, TEM and HRTEM images show that the nanofibrous morphology and chemical structure remain well preserved (Fig. S29 and S30, SI). The XRD pattern indicates only a slight reduction in crystallinity without any phase transformation. XPS spectra confirm that the valence states of all elements remain essentially unchanged. (Fig. S31, SI). Collectively, these results firmly establish $RuCoMoO_x$ NFs as a highly efficient and durable OER electrocatalyst, demonstrating great potential as a bifunctional catalyst for overall water splitting applications.

To elucidate the origin of the enhanced catalytic activity, systematic DFT calculations are conducted on a RuO_2 (110)/$CoMoO_4$ (002) heterojunction model (Fig. 5a). Differential charge density analysis demonstrates pronounced interfacial charge redistribution, characterized by electron accumulation on the RuO_2 side (yellow isosurfaces) and depletion on the $CoMoO_4$ side (cyan isosurfaces), confirming directional electron transfer from $CoMoO_4$ to RuO_2 across the heterojunction (Fig. 5b). Bader charge analysis quantifies this electron transfer as 5.34 e^-, which is further corroborated by the plane-averaged differential charge density profile along the *Z*-axis (Fig. 5c). Collectively, these results provide compelling evidence of substantial electronic structure modulation induced by heterojunction formation. The adsorption energies for the key OER intermediates (*OH, *O, and *OOH) are computed at Co, Mo and Ru sites on the $RuO_2/CoMoO_4$ heterojunction (Fig. 5d). According to the Gibbs free–energy diagram, the Co site emerges as the most favorable active center for the OER, where

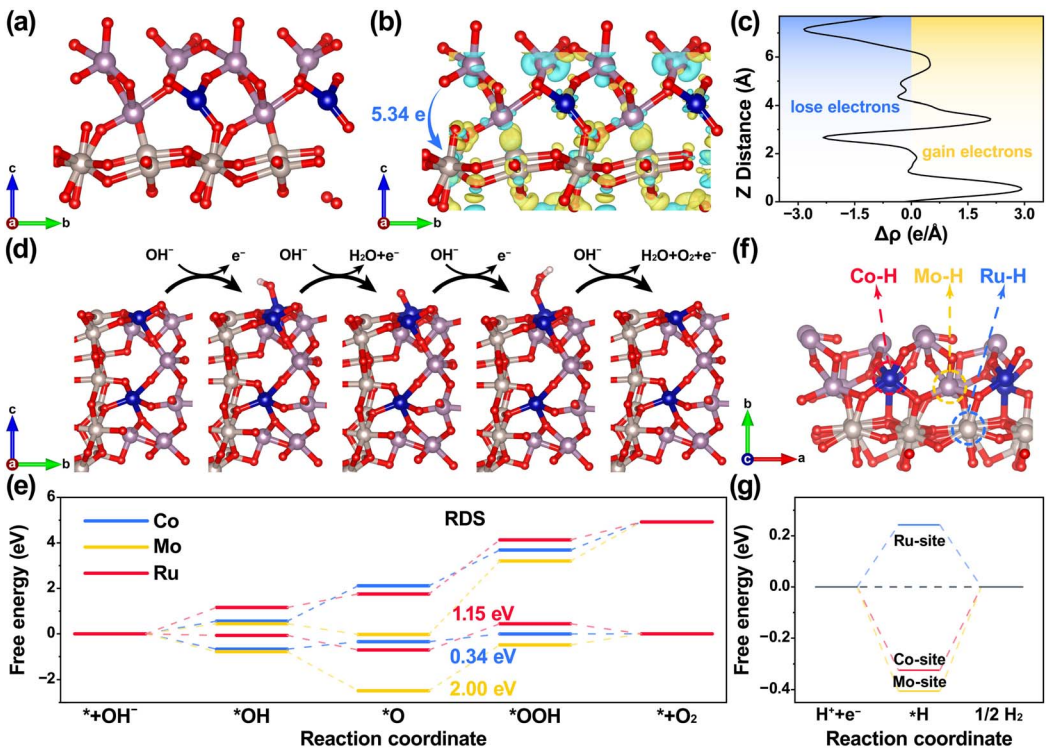

Fig. 5 DFT analysis of the $RuO_2/CoMoO_4$ heterojunction. (a) Atomic structure of the $RuO_2/CoMoO_4$ heterojunction model. (b) Differential charge density isosurfaces (yellow: charge accumulation; cyan: depletion). (c) Planar-averaged differential charge density along the *z*-axis. (d) Proposed OER reaction pathway on the heterojunction. (e) Calculated Gibbs free energy diagram for OER intermediates at $U = 0$ V and $U = 1.23$ V. (f) Atomic configurations of *H adsorption sites. (g) Corresponding *H adsorption free energies (ΔG_{*H}).

the transformation from *O to *OOH serves as the rate-determining step (RDS) with an energy barrier of only 0.34 eV, much lower than those at the Mo (2.00 eV) and Ru (1.15 eV) sites, accounting for the superior OER kinetics observed at the Co site (Fig. 5e). For the HER, the Ru site exhibits a near-optimal H* adsorption free energy ($\Delta G_{*H} = 0.24$ eV), outperforming the Co (−0.32 eV) and Mo (−0.41 eV) sites, thereby enabling highly favorable *H adsorption–desorption dynamics (Fig. 5f and g). Thus, the Co and Ru sites function as highly active centers for the OER and HER, respectively. This site-specific functionalization, driven by interfacial charge engineering, underpins the exceptional synergistic bifunctional performance of the RuO_2/$CoMoO_4$ heterojunction.

To assess the OWS performance of the $RuCoMoO_x$ NFs under industrial current density conditions, a two-electrode electrolyzer is assembled using $RuCoMoO_x$ NFs as both the cathode and anode (Fig. 6a). The $RuCoMoO_x$ NFs||$RuCoMoO_x$ NFs electrolyzer requires only 1.53 V to reach 10 mA cm^{-2}, significantly lower than the 1.58 V required by the commercial Pt/C||commercial RuO_2 electrolyzer (Fig. 6b). Furthermore, the $RuCoMoO_x$ NFs||$RuCoMoO_x$ NFs system exhibits superior activity, as evidenced by a smaller activation overpotential region compared to the commercial counterpart (Fig. 6c and S32a, SI). In addition, this configuration outperforms most reported bifunctional electrocatalyst-based electrolyzers (Fig. 6d and Table S4). The faradaic efficiencies (FEs) for both the HER and the OER are measured at 100 mA cm^{-2} using the water displacement method to assess the practical efficiency of the electrolyzer. The $RuCoMoO_x$ NFs||$RuCoMoO_x$ NFs system delivers FEs of 102.9% for the HER and 100.2% for the OER, surpassing those of commercial Pt/C||commercial RuO_2 (101.3% for the HER and 79.8% for the OER), respectively (Fig. 6e and S32b, SI). Moreover, long-term stability tests conducted at an industrial current density of 1 A cm^{-2} reveal that the $RuCoMoO_x$ NFs||$RuCoMoO_x$ NFs system retains stable current density after 60 h of continuous operation. In contrast, commercial Pt/C||commercial RuO_2 shows a significant reduction in its current density after more than 20 h under identical conditions (Fig. 6f). These results underscore the outstanding

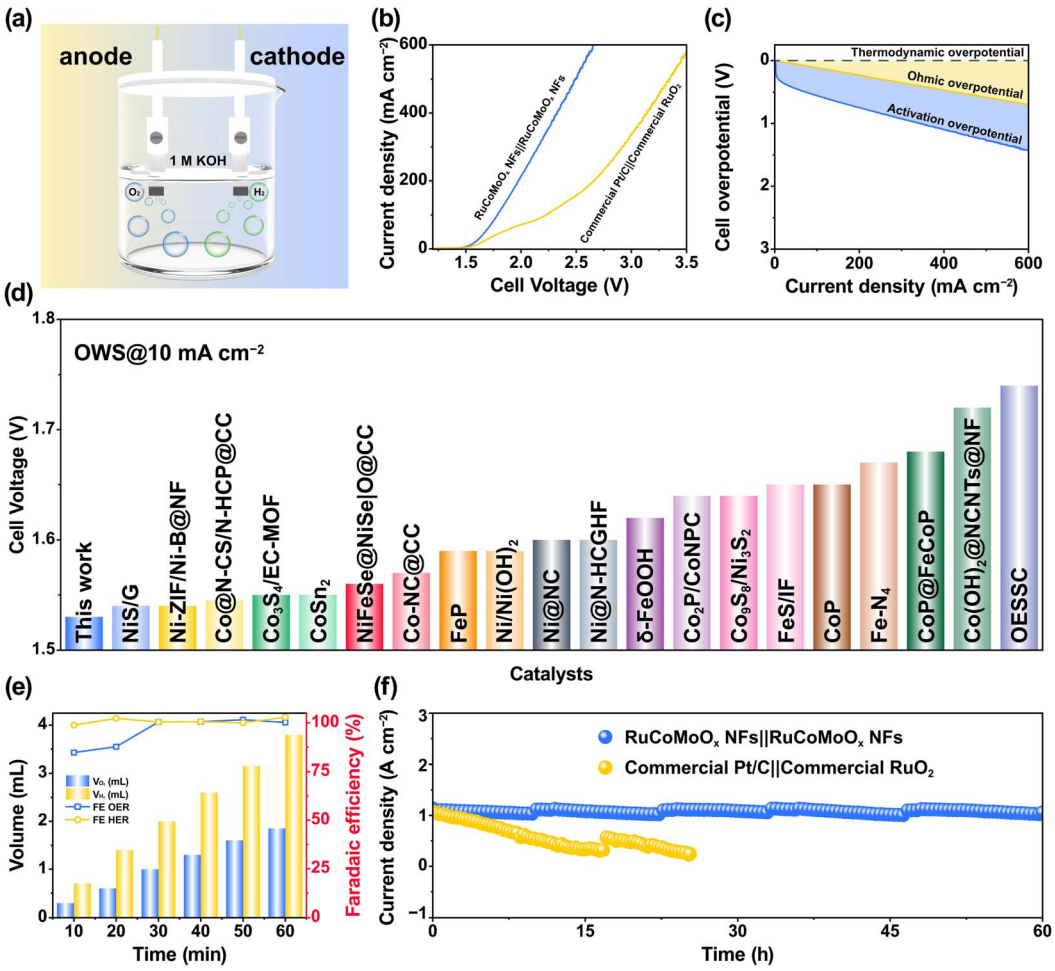

Fig. 6 Overall water splitting performance in a two-electrode system. (a) Schematic of the alkaline electrolyzer. (b) LSV curves of overall water splitting for $RuCoMoO_x$ NFs||$RuCoMoO_x$ NFs and commercial Pt/C||commercial RuO_2 electrolyzers. (c) Contributions of ohmic overpotential and activation overpotential. (d) Cell voltages required to achieve 10 mA cm^{-2} compared with state-of-the-art alkaline electrolyzers. (e) FE of the $RuCoMoO_x$ NFs||$RuCoMoO_x$ NFs electrolyzer. (f) Chronopotentiometric stability test of electrolyzers at 1 A cm^{-2}.

durability and industrial applicability of $RuCoMoO_x$ NFs-based water electrolysis for sustainable H_2 production.

Conclusion

In summary, $RuCoMoO_x$ NFs incorporating $RuO_2/CoMoO_4$ heterojunctions are successfully synthesized *via* electrospinning followed by controlled calcination. The optimized nanofibrous architecture facilitates efficient charge transfer, endowing the material with outstanding bifunctional activity, achieving ultralow overpotentials of 274.8 mV for the HER and 367.9 mV for the OER at 1 A cm^{-2}, while maintaining excellent durability at such ampere-level current densities. When assembled into an alkaline electrolyzer, the $RuCoMoO_x$ NFs||$RuCoMoO_x$ NFs system requires only 1.53 V to deliver 10 mA cm^{-2} and maintains stable current density after 60 h of operation under ampere-level conditions. DFT calculations reveal that interfacial electron redistribution across the $RuO_2/CoMoO_4$ heterojunction optimizes the adsorption energetics of key intermediates at Ru and Co sites, thereby enhancing the HER and OER performance, respectively. This study provides valuable design principles for developing robust noble-metal-lean Ru-based electrocatalysts that meet the practical demands of industrial alkaline water electrolysis.

Author contributions

L. Z. performed the experiments, conducted theoretical calculations, and wrote the manuscript. M. X. conducted the experiments, collected and analyzed data for all the revision. S. R., L. D., S. Z. and L. H. analyzed the data. W. L. and X. L. offered supervision, project administration and writing-review & editing. W. S. supervised the project. X. L. provided the funding acquisition.

Conflicts of interest

The authors declare no conflict of interest.

Data availability

The data supporting this article have been included as part of the supplementary information (SI). Supplementary information: comprehensive experimental protocols, along with supplementary characterization results and electrochemical performance metrics. See DOI: https://doi.org/10.1039/d6sc02482c.

Acknowledgements

This work was financially supported by the National Natural Science Foundation of China (52273056) and the Science and Technology Development of Jilin Province, China (YDZJ202501ZYTS305).

References

1 Z. W. Seh, J. Kibsgaard, C. F. Dickens, I. Chorkendorff, J. K. Nørskov and T. F. Jaramillo, *Science*, 2017, **355**, eaad4998.
2 J. Chow, R. J. Kopp and P. R. Portney, *Science*, 2003, **302**, 1528–1531.
3 L. Li, P. Wang, Q. Shao and X. Huang, *Chem. Soc. Rev.*, 2020, **49**, 3072–3106.
4 W. Li, C. Wang and X. Lu, *J. Mater. Chem. A*, 2021, **9**, 3786–3827.
5 W. Li, C. Wang and X. Lu, *Nano Lett.*, 2024, **24**, 11779–11792.
6 M. Rafique, T. Yao, S. Ma, Y. Xu, L. Li, J. Han, Q. Fu, W. Li, Z. Yuan, K. Wang and B. Song, *Adv. Funct. Mater.*, 2025, e12495.
7 J. Baek, M. D. Hossain, P. Mukherjee, J. Lee, K. T. Winther, J. Leem, Y. Jiang, W. C. Chueh, M. Bajdich and X. Zheng, *Nat. Commun.*, 2023, **14**, 5936.
8 K. B. Ibrahim, G. P. Darshan, G. Benetti, P. Kumar, E. Rodríguez-Castellón, T. A. Shifa, E. Moretti and A. Vomiero, *Adv. Sustainable Syst.*, 2025, 2500385.
9 W. Yang, Z. Wang, J. Zhang, L. Jia, J. Li, X. Chen, X. Liu, H. Zhang, J. Lin, M. Zhao and Q. Chen, *Angew. Chem., Int. Ed.*, 2025, **64**, e202509768.
10 H. He, D. Zhu, C. Huang, G. Chang, Y. Qian, M. Ran, A. Hu, X. Chen and Q. Tang, *ACS Appl. Mater. Interfaces*, 2025, **17**, 29535–29545.
11 K. Du, L. Zhang, J. Shan, J. Guo, J. Mao, C.-C. Yang, C.-H. Wang, Z. Hu and T. Ling, *Nat. Commun.*, 2022, **13**, 5448.
12 H. Xu, H. Shang, C. Wang and Y. Du, *Coord. Chem. Rev.*, 2020, **418**, 213374.
13 S. Fu, Y. Ma, X. Yang, X. Yao, Z. Jiao, L. Cheng and P. Zhao, *Appl. Catal., B*, 2023, **333**, 122813.
14 F. Luo, W. Liu, Y. Liu, P. Yu, X. Jiang and S. Chen, *Chem. Eng. J.*, 2023, **475**, 146140.
15 C. Xu, Y. Hong, Z. Li, X. Di, W. Wang, X. Dong and X. Mou, *Coord. Chem. Rev.*, 2025, **523**, 216287.
16 Y. Zhang, J. Dong, T. Sun, X. Zhang, J. Chen and L. Xu, *Small*, 2024, **20**, 2305889.
17 J. Wang, H. Yang, F. Li, L. Li, J. Wu, S. Liu, T. Cheng, Y. Xu, Q. Shao and X. Huang, *Sci. Adv.*, 2022, **8**, eabl9271.
18 Y. Liu, L. Wu, Y. Wang, L.-W. Shen, G. Tian, L. Cui, L. Qin, L. Zhou, Y. Zhang, F. Rosei and X.-Y. Yang, *ACS Nano*, 2025, **19**, 2715–2725.
19 B. Fei, Z. Chen, Y. Ha, R. Wang, H. Yang, H. Xu and R. Wu, *Chem. Eng. J.*, 2020, **394**, 124926.
20 K. Chi, X. Tian, Q. Wang, Z. Zhang, X. Zhang, Y. Zhang, F. Jing, Q. Lv, W. Yao, F. Xiao and S. Wang, *J. Catal.*, 2020, **381**, 44–52.
21 W. Jia, Q. Lu, T. Tian, G. Pan, R. Tan, B. He and J. Liu, *Nanoscale*, 2024, **16**, 18076–18085.
22 X. Zhong, Y. Chen, T. Gan, Y. Huang, J. Li and S. Zhang, *Nano Res.*, 2025, **18**, 94907204.
23 B. Shi and X. Lu, *Chem. Sci.*, 2025, **16**, 17568–17594.

24 N. Song, S. Ren, Y. Zhang, C. Wang and X. Lu, *Adv. Funct. Mater.*, 2022, **32**, 2204751.
25 L. Zhang, W. Li, S. Ren, W. Song, C. Wang and X. Lu, *Adv. Energy Mater.*, 2025, **15**, 2403136.
26 X. Yu, R. B. Araujo, Z. Qiu, E. Campos dos Santos, A. Anil, A. Cornell, L. G. M. Pettersson and M. Johnsson, *Adv. Energy Mater.*, 2022, **12**, 2103750.
27 W. Li, W. Gou, L. Zhang, M. Zhong, S. Ren, G. Yu, C. Wang, W. Chen and X. Lu, *Chem. Sci.*, 2024, **15**, 11890–11901.
28 Y. Wang, Q. Jiang, S. Ren, J. Xu, Y. Wang, M. Zhong and X. Lu, *Adv. Mater.*, 2025, **37**, 2504922.
29 X. Yu, M. Xia, R. Qi, Y. Wang, M. Gao, M. Zhong and X. Lu, *Chem. Sci.*, 2025, **16**, 10042–10050.
30 Q. Lin, R. Zhang, X. Zhang, S. Li, J. Dai, S. Li, Z. Wang, D. Liang, H. Fu and X. Zhang, *Catal. Lett.*, 2025, **155**, 67.
31 Y. Fan, W. Ma, J. He and Y. Du, *RSC Adv.*, 2017, **7**, 36193–36200.
32 W. Li, L. Zhang, L. Ma, J. Wang, R. Qi, Y. Pang, M. Xu, C. Zhao, C. Wang, M. Gao and X. Lu, *Nano Lett.*, 2025, **25**, 443–452.
33 Y. You, H. Chen, J. Guo, Z. Feng, J. Zhan, F. Yu and L.-H. Zhang, *Appl. Catal., B*, 2025, **363**, 124837.
34 H. Chen, X. Zhang, S. Geng, S. Song and Y. Wang, *Small Methods*, 2022, **6**, 2200636.
35 H. Wang, X. Shao, Y. Wei, X. Ai, J. Yu, N. Xiao, R. Gan and Y. Qu, *Appl. Catal., B*, 2025, **367**, 125110.
36 J. Zhang, Q. Chen, G. Wang, X. An, J. Zhang, Q. Liu, L. Xie, X. Li, W. Yao and Q. Kong, *Chem. Eng. J.*, 2024, **498**, 155474.
37 W. Jiang, M. Su, Y. Zheng and T. Fei, *ACS Appl. Mater. Interfaces*, 2024, **16**, 7406–7414.
38 W. Zhang, X. Xiao, L. Zheng and C. Wan, *Can. J. Chem. Eng.*, 2015, **93**, 1594–1602.
39 W. Tang, S. Zhu, H. Jiang, Y. Liang, Z. Li, S. Wu and Z. Cui, *J. Colloid Interface Sci.*, 2022, **625**, 606–613.
40 T. Chen, Y. Wu, H. Zhang, X. He, Z. Zhu, Y. Wei, C. Li, H. Zhu, S. Yu and W. Dong, *ACS Sustainable Chem. Eng.*, 2024, **12**, 9078–9090.
41 Y. Wang, X. Lei, B. Zhang, B. Bai, P. Das, T. Azam, J. Xiao and Z.-S. Wu, *Angew. Chem., Int. Ed.*, 2024, **63**, e202316903.
42 Y. Li, Q. Zhang, X. Zhao, H. Wu, X. Wang, Y. Zeng, Q. Chen, M. Chen and P. Liu, *Adv. Funct. Mater.*, 2023, **33**, 2214124.
43 Y. Gao, D. Zheng, Q. Li, W. Xiao, T. Ma, Y. Fu, Z. Wu and L. Wang, *Adv. Funct. Mater.*, 2022, **32**, 2203206.
44 W. Li, R. Liu, G. Yu, X. Chen, S. Yan, S. Ren, J. Chen, W. Chen, C. Wang and X. Lu, *Small*, 2024, **20**, 2307164.
45 W. Chen, B. Wu, Y. Wang, W. Zhou, Y. Li, T. Liu, C. Xie, L. Xu, S. Du, M. Song, D. Wang, Y. Liu, Y. Li, J. Liu, Y. Zou, R. Chen, C. Chen, J. Zheng, Y. Li, J. Chen and S. Wang, *Energy Environ. Sci.*, 2021, **14**, 6428–6440.
46 H. Jin, X. Chen, Y. Da, L. Fan, R. Jiang, Y. Xiao, B. Yao, Q. He, Y. Yu and W. Chen, *J. Am. Chem. Soc.*, 2025, **147**, 3874–3884.
47 X. Zhao, H. Zheng, H. Sun, M. Chen, B. Wang, Q. Lu, B. Xiao, T. Zhou, D. Li, G. Qiu, J. Zhang, Y. Zhang, X. Xu, T. He and Q. Liu, *Adv. Energy Mater.*, 2026, **16**, e04983.
48 H. Sun, Z. Luo, M. Chen, T. Zhou, B. Wang, B. Xiao, Q. Lu, B. Zi, K. Zhao, X. Zhang, J. Zhao, T. He, J. Zhang, H. Cui, F. Liu, C. Wang, D. Wang and Q. Liu, *ACS Nano*, 2024, **18**, 35654–35670.